Virtual simulation of maneuvering captive tests for a surface vessel

Ahmad Hajivand and S. Hossein Mousavizadegan

Department of Maritime Engineering, Amirkabir University of Technology, Tehran, Iran

ABSTRACT: *Hydrodynamic derivatives or coefficients are required to predict the maneuvering characteristics of a marine vehicle. These derivatives are obtained numerically for a DTMB 5512 model ship by virtual simulating of captive model tests in a CFD environment. The computed coefficients are applied to predict the turning circle and zig-zag maneuvers of the model ship. The comparison of the simulated results with the available experimental data shows a very good agreement among them. The simulations show that the CFD is precise and affordable tool at the preliminary design stage to obtain maneuverability performance of a marine vehicles.*

KEY WORDS: Maneuvering; Computational fluid dynamics (CFD); Hydrodynamic derivatives; Oblique towing test (OTT); Planar motion mechanism (PMM).

INTRODUCTION

Maneuverability is an important quality of marine vehicles. It should be controlled during various design stages and at the end of building the vessels. It has influences on efficiency and safety of marine transportation system. Maneuvering of a marine vehicle is judged based on its course keeping, course changing and speed changing abilities. International Maritime Organization (IMO) recommends criteria to investigate ship and other marine vehicles maneuvering quality (IMO, 2002a; 2002b).

Maneuverability of a ship or another marine vehicle may be predicted by model tests, or mathematical models or both. Mathematical models for prediction of marine vehicle's maneuverability may be divided into two main categories called as hydrodynamic models, and response models. The hydrodynamic models are of two types and recognized as the hydrodynamic coefficient models such as Abkowitz (Abkowitz, 1969) model and modular models such as MMG (Yoshimura, 2005) model. The Abkowitz model is based on the Taylor series expansion of hydrodynamic forces and moments about suitable initial conditions. The MMG model decomposes hydrodynamic forces and moments into three components namely: the bare hull; rudder; and propeller and also considers the interaction between them. The response model investigates the relationship for the motion responses of the vehicle to the rudder action and used to investigate the course control problems (Nomoto, 1960).

The hydrodynamic models, such as the Abkowitz formulation, contain several derivatives that are known as the hydrodynamic coefficients. These hydrodynamic coefficients should be determined in advance to proceed into the predicting the maneuvering characteristics of a marine vehicle. These hydrodynamic coefficients are named as added mass and damping

---

Corresponding author: *S. Hossein Mousavizadegan*, e-mail: *hmousavi@aut.ac.ir*

coefficients. All of them are functions of the geometry of the vessel and the added mass coefficients depend on the acceleration of the vessel while the damping coefficients are velocity dependent. The added mass coefficients can be computed through the solution of the non-viscous fluid flow around the vessel. The damping coefficients are due to the wave formation in the free surface of the water and the effect of the viscosity. The total damping coefficients may be obtained through the solution of viscous fluid flow around the vessel.

There are several methods to obtain hydrodynamic coefficients such as analytical approach, semi empirical formulas, captive model tests, and Computational Fluid Dynamics (CFD). Analytical approach is based on potential flow theory and therefore the effect of viscosity is ignored. It can provide the added mass coefficients and the part of damping coefficients due to the wave formation on the free surface of water. Semi empirical formulas are obtained using linear regression analysis of captive model test data. They can provide the coefficients only for some specific geometrical shape and are inaccurate when the particulars of vessel are outside of the database. The captive model tests provide the hydrodynamic coefficients through the running the tests: Rotating Arm Test (RAT) or Circular Motion Test (CMT) and Planar Motion Mechanism (PMM) test. The PMM test is done in a towing tank and the RAT is run in a maneuvering basin.

The PMM tests may be done in a straight path when the model has a drift angle with the fluid flow. Such a test is called as Oblique Towing Test (OTT) and provides the damping coefficients depending on the translational velocities. The oblique towing test is a stationary test since the model is running with a constant velocity in a straight path and therefore, there is no acceleration involved. The PMM tests may also be done in a sinusoidal path with various orientation of the body. These types of tests are also called as dynamic tests since the body is acted by inertia forces. The dynamic tests can provide the acceleration and velocity dependent hydrodynamic coefficients. Two of the most important PMM tests are pure sway and pure yaw tests. These types of model tests need special equipment and are expensive, time consuming and their results include the scaling effects due to inconsistency of Reynolds number between the ship and the model.

CFD can also be used to obtain the maneuvering hydrodynamic coefficients of a marine vehicle such as a ship by virtual simulation of the captive model tests. CFD methods use the Navier-Stokes equations to model a given fluid flow. There are various approaches to solve the fluid flow equation for a viscous flow such as the flow around a maneuvering ship. These methods may be listed as Direct Numerical Simulation (DNS), large eddy simulation (LES) and Reynolds averaged Navier-Stokes (RANS) methods. DNS and LES need very high computational capacity. RANS models are time-averaged formulations of fluid flow motion equations and are based on statistical tool known as Reynolds decomposition.

Application of RANS to solve the maritime problems goes back to (Wilson et al., 1998) who have obtained unsatisfactory results. By the increasing growth of computing capacities and recent progress in RANS models, stunning advances in this field are achieved. Nowadays, CFD is crucial tool for various aspect of a marine vehicle hydrodynamics such as ship resistance and propeller performance not only for research but also as a design tool. One of the most recently and important application of CFD in marine industry is computation of hydrodynamic coefficients of marine vehicles by simulating the captive model tests. Sarkar et al. (1997) develop a new computationally efficient technique to simulate the 2-D flow over axisymmetric AUVs by using the CFD software PHOENICS. Nazir et al. (2010) and, Zhang et al. (2010) apply the commercial CFD software Fluent to obtain hydrodynamic coefficients of 3-D fins and an AUV, respectively. Tyagi and Sen (2006) compute transverse hydrodynamic coefficients of an AUV using a CFD commercial software. The hydrodynamic forces and moments on an AUV due to the deflection of control surfaces are investigated using ANSYS Fluent commercial CFD software by Dantas and de Barros (2013). Ray et al. (2009) apply CFD software Fluent to compute linear and nonlinear hydrodynamic coefficients of the DARPA Suboff submarine in an unrestricted fluid flow. The above presented studies use CFD methods to calculate the hydrodynamic coefficients of underwater marine vehicles. However, the CFD methods are also used to predict the hydrodynamic coefficients of ships. Stern et al. (2011) review the several works have been done in SIMMAN workshop to simulate captive maneuvering tests. Simonsen et al. (2012) simulate the fixed OTT for the KCS model by employing the commercial CFD software STAR-CCM+ to calculate the hydrodynamic coefficients. Hajivand and Mousavizadegan (2015) simulate OTT for the DTMB 5512 model by applying OpenFOAM software. They study the effect of dynamic trim and sinkage on hydrodynamic coefficients.

The Star-CCM+ software is applied to simulate the OTT and dynamic PMM tests for a DTMB 5512 ship which is a 1/46.6 scale geosym of DTMB model 5415 shown in Fig. 1. Particulars of the model are given in Table 1. The OTT simulations are done for wide range of the drift angles to obtain nonlinear damping coefficients. The dynamic PMM test simulations are done

with different yaw rates, sway velocities and motion frequencies. The simulation pattern is set based on experiments that are performed for a combatant ship at Iowa Institute of Hydraulic Research (IIHR) towing tank (Yoon, 2009). The standard industrial model k-ε is used to consider the turbulent effects. Grid convergence is performed, locally and globally, for OTT and PMM simulations. By simulating the OTT and PMM captive maneuvers, the linear and nonlinear damping coefficients and added mass coefficients are calculated. Then, these coefficients are applied to simulate the turning and zig-zag maneuvers. The results are compared with the available data based on experimental tests. It is found that the computed results comply with the existing experimental results.
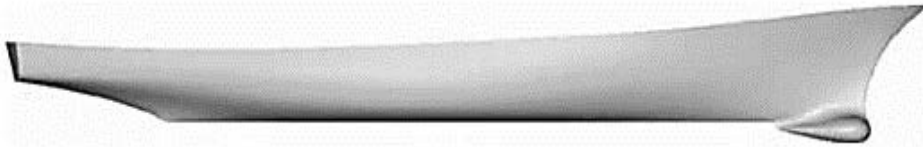

Fig. 1 DTMB 5512 bare hull model (Yoon, 2009).

Table 1 Geometrical data for DTMB 5512 model (Yoon, 2009).

L_{PP}	$[m]$	3.048
B	$[m]$	0.410
T	$[m]$	0.136
∇	$[m^3]$	0.086
S	$[m^2]$	1.371
C_B	[-]	0.506

MANEUVERING EQUATION

An earth fixed reference frame system O-$x_E y_E z_E$ and a body-fixed coordinate system o-xyz are defined as shown in Fig. 2. If it is assumed the body is moving in horizontal plane o-xy, the origin o coincides with the center of mass and the coordinate system coincide with the principle axes of inertia. The motion equation may be given as follows in horizontal plane for a ship in the body-fixed coordinate system.

$$m(\dot{u} - rv) = X \qquad (1)$$

$$m(\dot{v} + ru) = Y \qquad (2)$$

$$I_z \dot{r} = N \qquad (3)$$

where Eq. (1), (2) and (3) are surge, sway, and yaw motion equations, respectively. The notation m is the mass of the body, I_z is the mass moment of inertia of the body about z-axis, u and v are the velocities of the body along x and y directions, respectively. The notations $\dot{u}$ and $\dot{v}$ are the acceleration of the body along x and y directions, respectively, and r and $\dot{r}$ are the angular velocity and angular acceleration around the z-axis of the body, respectively.
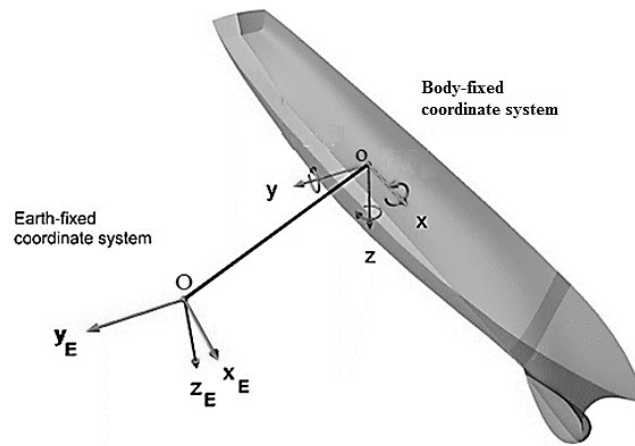
Fig. 2 Earth-fixed and body-fixed coordinate system (Yoon, 2009).

The notations X and Y are external forces along x and y axis, respectively and N is the external moment about the z-axis. A part of these external forces and moment are hydrodynamic forces and moment that arise due to the interaction of the body with the surrounded water. The hydrodynamic forces and moment may be written as follows according to the Abkowitz model with the assumption that the body is moving with a constant speed, U_c, and the control surfaces are in neutral position.

$$
\begin{aligned}
X &= X_{\dot{u}}\dot{u} + X_u \delta u + X_{uu}\delta u^2 \\
&+ X_{vv}v^2 + X_{rr}r^2 + X_{vvu}v^2\delta u \\
&+ X_{rru}r^2\delta u + X_{vr}vr + X_{vru}vr\delta u
\end{aligned}
\tag{4}
$$

$$
\begin{aligned}
Y &= Y_u \delta u + Y_{uu}\delta u^2 + Y_{uuu}\delta u^3 \\
&+ Y_{\dot{v}}\dot{v} + Y_{\dot{r}}\dot{r} + Y_v v + Y_{vvv}v^3 \\
&+ Y_{vrr}vr^2 + Y_{vu}v\delta u + Y_{vuu}v\delta u^2 + Y_r r \\
&+ Y_{rrr}r^3 + Y_{rvv}rv^2 + Y_{ru}r\delta u + Y_{ruu}r\delta u^2
\end{aligned}
\tag{5}
$$

$$
\begin{aligned}
N &= N_u \delta u + N_{uu}\delta u^2 + N_{uuu}\delta u^3 \\
&+ N_{\dot{v}}\dot{v} + N_{\dot{r}}\dot{r} + N_v v + N_{vvv}v^3 \\
&+ N_{vrr}vr^2 + N_{vu}v\delta u + N_{vuu}v\delta u^2 + N_r r \\
&+ N_{rrr}r^3 + N_{rvv}rv^2 + N_{ru}r\delta u + N_{ruu}r\delta u^2
\end{aligned}
\tag{6}
$$

where $\delta u = u - U_c$ and all notations such as X_u, Y_{vvv}, N_{ru}, etc at right hand side of (4), (5) and (6) are hydrodynamic derivatives or coefficients.

PMM test can provide explicitly all maneuvering coefficients. The OTT provides Y_v and N_v, and nonlinear, X_{vv}, Y_{vvv} and N_{vvv}. The dynamic PMM tests can provide all the hydrodynamic derivatives given in (4), (5) and (6). These coefficients may also be obtained by simulating the OTT and dynamic PMM tests in a CFD environment virtually. In other word, these coefficients may also be obtained by modeling the fluid flow motion around the body.

FLUID FLOW MODELING

The unsteady viscous flow around a marine vehicle is governed by the Navier-Stokes equations. Navier-Stokes equations can be applied to both laminar and turbulent flow but a very fine meshing is necessary to capture all the turbulence effects in a

turbulent flow regime. The Reynolds-averaged Navier-Stokes (RANS) equations can also be applied to model the turbulent flow. The RANS equations are obtained based on statistical tools known as Reynolds decomposition where the flow parameters are decomposed into time-averaged and fluctuation parts, i.e. $u = \bar{u} + u'$ and $p = \bar{p} + p'$ where $\bar{u}$ and $\bar{p}$ are the time-averaged and u' and p' are the fluctuation velocity and pressure, respectively. The RANS equations may be given as follows for an incompressible flow (Ferziger and Peric, 2002).

$$\frac{\partial(\rho \bar{u}_i)}{\partial t} + \frac{\partial}{\partial x_j}(\rho \bar{u}_i \bar{u}_j + \rho \overline{u_i' u_j'}) = -\frac{\partial \bar{p}}{\partial x_i} + \rho g_i + \frac{\partial}{\partial x_j}\left(\mu\left(\frac{\partial \bar{u}_i}{\partial x_j} + \frac{\partial \bar{u}_j}{\partial x_i}\right)\right) \tag{7}$$

$$\frac{\partial(\rho \bar{u}_i)}{\partial x_i} = 0 \tag{8}$$

where ρ is the fluid density, g_i is the components of gravitational acceleration, and μ is fluid dynamic viscosity. The notation $\rho \overline{u_i' u_j'}$ is the Reynolds stress tensor components. The Reynolds stress tensor components are estimated by turbulence models which are approximations to the physical phenomena of turbulence.

The k-ε is used to model the turbulence effects. The two equation turbulence model k-ε is the most frequently used turbulence model where the effect of Reynolds stresses is considered as an additional eddy viscosity which is a property of the flow. Eddy viscosity expressed as:

$$\mu_t = \rho C_\mu \frac{k^2}{\varepsilon} \tag{9}$$

where k is the turbulence kinetic energy per unit mass, ε is the rate of the dissipation of the turbulence kinetic energy per unit mass and C_μ is a dimensionless constant of a normal value of 0.09. The turbulent kinetic energy and the dissipation rate are calculated from the solution of transport equations (Ferziger and Peric, 2002). The VOF approach is applied to capture the effect of the free surface. Transport equation is solved for volume fraction to track free surface. At free surface the fluid density, ρ, and viscosity, μ, are calculated as follows (Hirt and Nichols, 1981).

$$\rho = \rho_{air} c + \rho_{water} (1-c) \tag{10}$$

$$\mu = \mu_{air} c + \mu_{water} (1-c) \tag{11}$$

where c is volume fraction that is defined as (V_{air} / V_{total}) and is obtained by solution of the advection equation.

$$\frac{\partial c}{\partial t} + \nabla \cdot (cU) = 0 \tag{12}$$

Mesh generation

Finite Volume Method (FVM) is the common approach to solve RANS equations in computational domain. The computational domain is discretized to finite control volumes. The computational domain is selected sufficiently large to avoid back flow at high drift angles. Distances of the inlet and outlet boundary from ship center are considered 1.5L_{PP} and 3L_{PP}, respectively. The side boundaries are located at 2.5L_{PP} and the top and bottom boundary is located at 1L_{PP} and 2L_{PP} from the free surface, respectively (Fig. 3).

There are different meshing strategies to discretize the computational domain (Seo et al., 2010). Simulations are done on unstructured trimmed meshes. The trimmer meshing strategy is a proficient and strong method that generates high quality mesh with lowest grid skewness. Local refinement is applied where wave formation is predictable. The overall view of the mesh around the ship bow and free surface is displayed in Figs. 4 and 5, respectively. The simulation of PMM tests should be done in a moving meshing system. Therefore, computational domain for PMM test is discretized by using overset mesh approach. Overset technique divided computational domain to a background region surrounding the entire solution domain and an overset region including the moving ship hull within the domain. The overall view of the overset mesh is displayed in Fig. 6.
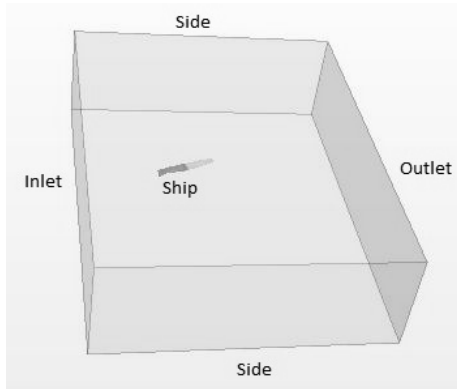

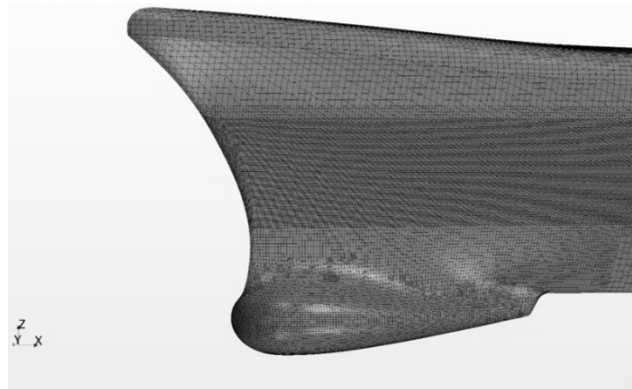Fig. 3 Illustration of computational domain.
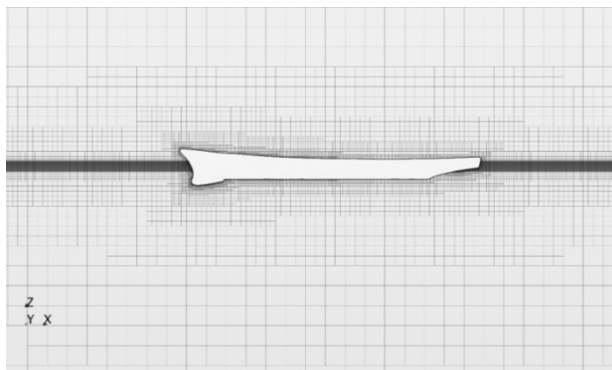

Fig. 4 Mesh around the bow.

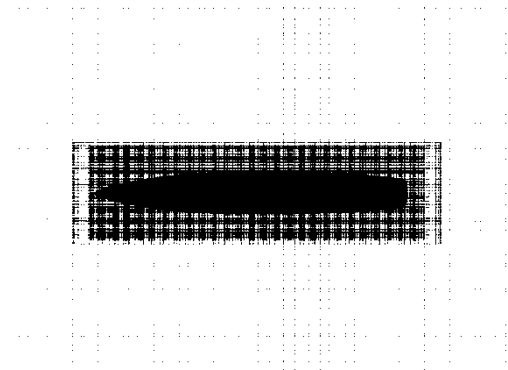Fig. 5 Mesh refinement around free surface.

Fig. 6 Overset mesh around hull.

Prism layer refinement is applied around the ship hull to improve the accuracy of the solution in the boundary layer region. The turbulent flow inside the boundary layer is approximated by wall functions. Park et al. (2013) investigate implementation of the wall function for the prediction of ship resistance. High y^+ wall treatment that is based on equilibrium turbulent boundary layer theory is used as wall function approach. The mean value of y^+ on the hull surface is around 30 that show refinement of prism layer be well. Distribution of y^+ for fine mesh on hull is shown in Fig. 7.

Fig. 7 Distribution of y+ for fine mesh on hull.

Boundary conditions

Appropriate boundary conditions on the free surface, fluid domain boundaries and ship's hull must be applied to create a well-posed system of equations. The boundaries of domain split into patches as shown in Fig. 3. The boundary conditions are chosen such that to avoid back flow and lateral wall effects. On solid surfaces such as the body surface there are two kinematic boundary conditions. The first one is the no flow through the surface, and the second one is a no slip on the surface. These are applied on the instantaneous wetted surface of the ship. On the free surface of water, the constant pressure and no shear stress conditions are applied. These conditions are applied on the unknown free surface, which must also be determined as part of the solution. On the bottom boundary for finite depth there is a kinematic condition, or in infinitely deep water the disturbance velocities must go to zero. At infinity, there is a radiation condition of outgoing waves on the ship-generated waves.

GRID CONVERGENCE

Spatial and temporal sensitivity analysis is the most straight-forward and the most consistent technique for determining the order of discretization error in numerical simulation. In other words, numerical results can be considered as precise and valid if its solution be independent of the grid size and time-step.

A grid convergence study involves implementation solution on the CFD model, with sequentially refined grids of reduced mesh size, until the solutions become independent of the mesh size. Three different meshes with constant grid refinement factor in all three spatial directions, $r=h_2/h_1=h_3/h_2=1.4$, are employed. The notation h_i is a measure of the mesh discretization. Based on experiments, it is desirable that $r>1.3$, this reduces the errors arising from extrapolation. These cases are labeled s_1, s_2 and s_3 from finest to coarsest mesh.

The OTT is simulated with Star-CCM+ using these grids. The corresponding forces and moment are obtained for a drift angle $\beta = -6$ degree at $F_n = 0.28$. The number of meshes and calculated non-dimensional forces and moment coefficients are shown in Table 2. The forces and moment are made dimensionless with water density ρ, inflow speed u, lateral underwater area TL_{PP} and length between perpendiculars L_{PP}:

$$X' = \frac{F_X}{0.5\rho^2 TL_{PP}} \tag{13}$$

$$Y' = \frac{F_Y}{0.5\rho u^2 TL_{PP}} \tag{14}$$

$$N' = \frac{M_Z}{0.5\rho u^2 TL^2_{PP}} \tag{15}$$

Table 2 Dimensionless forces and moment for different grid (OTT).

Number of grids	X'	Y'	N'
1,360,061	-0.01811	0.02815	0.01120
2,533,357	-0.01765	0.02977	0.01325
6,00,9588	-0.01742	0.03060	0.01431

For dynamic simulations, mesh study are investigated for the pure sway with maximum sway velocity, $v_{max} = 0.385$ *m/s* and for the pure yaw with maximum yaw rate, $r_{max} = 0.45$ *rad/s*. Both conditions are perrformed at medium advance speed. The corresponding magnitude of forces and moment for each grid are calculated. Mesh numbers and non-dimensional maximum forces and moment for pure sway and pure yaw are shown in Table 3.

Convergence ratio defined as follows.

$$R = \frac{\varepsilon_{21}}{\varepsilon_{32}}$$

where

$\varepsilon_{21} = s_2 - s_1$ is the difference between solution of fine and medium grid;

$\varepsilon_{32} = s_3 - s_2$ is the difference between solution of medium and coarse grid.

The possible convergence situations are:

$R > 1$: Grid divergence

$R < 0$: Oscillatory convergence

$0 < R < 1$: Monotonic grid convergence

Table 3 Dimensionless forces and moment for different grid (PMM).

Pure sway			Pure yaw		
X'_{max}	Y'_{max}	N'_{max}	X'_{max}	Y'_{max}	N'_{max}
0.02322	0.11371	0.02812	0.0101	0.0081	0.00453
0.01908	0.11093	0.02669	0.00877	0.00764	0.00434
0.01760	0.10955	0.02598	0.00816	0.00742	0.00424

If grid convergence occurs, Richardson extrapolation also called h^2 extrapolation is used to estimate convergence rate. Order of discretization estimated as follows:

$$p = \frac{\ln\left(\varepsilon_{32} / \varepsilon_{21}\right)}{\ln(r)} \qquad (16)$$

where r is grid refinement factor. After that, Grid Convergence Index (GCI) is defined

$$GCI_{ij} = F_S \frac{\left|e_{ij}\right|}{r^P - 1}, \qquad (17)$$

where F_S is a safety factor with a value of $F_S = 1.25$ as recommends by Roache (1997) for convergence study with minimum three grids or more. The notation GCI indicates that computed value how far away from exact value. On the other hand, GCI is a measure of solution changes with more grid refinement. Small value of GCI means that the solution is in exact value range. Computed convergence ratio, order of discretization and GCI are illustrated in Table 4. Theoretical value for convergence is p=2. The difference is due to grid orthogonally, problem nonlinearities, turbulence modeling.

Table 4 Estimated convergence ratio, order of discretization and GCI for OTT and PMM tests.

	OTT			Pure sway			Pure yaw		
	X'_{max}	Y'_{max}	N'_{max}	X'_{max}	Y'_{max}	N'_{max}	X'_{max}	Y'_{max}	N'_{max}
R	0.50000	0.51235	0.51707	0.47716	0.49640	0.49650	0.45865	0.47826	0.52632
p	2.06004	1.98755	1.96025	2.19902	2.08150	2.08090	2.31661	2.19215	1.90760
GCI_{fine}	0.00029	0.00109	0.00142	0.00214	0.00170	0.00088	0.00065	0.00025	0.00014

For OTT the predicted water elevation along the plane at y=0.3 *m* and y=-0.3 *m* for the coarse, medium and fine grid is compared in Figs. 8 and 9, respectively. It is seen that difference between the water elevation of medium and fine grids is lower than difference between the water elevation of coarse and medium grids, especially at midship.
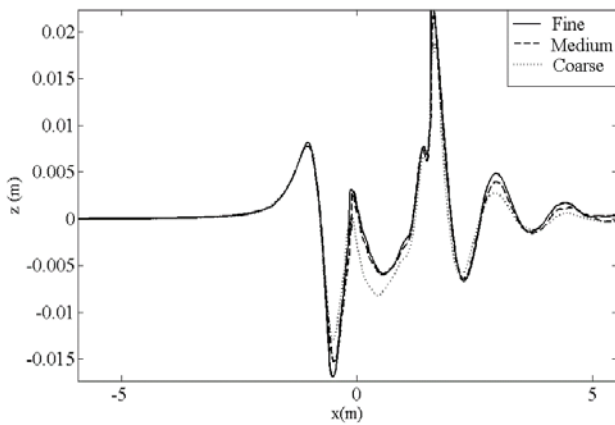

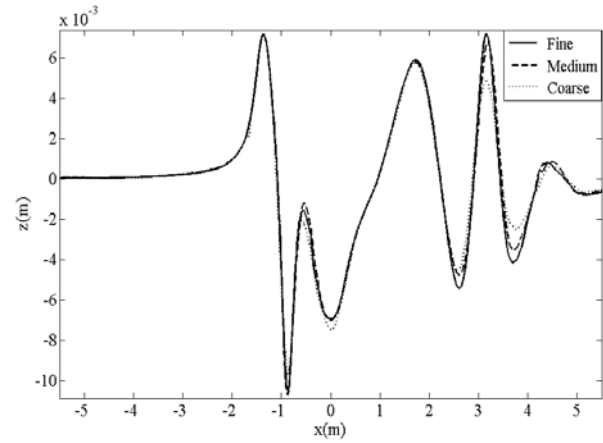Fig. 8 Comparison of water elevation along the cut at y=0.3 *m* for different grids for $\beta = 6°$ at $F_n = 0.28$.

Fig. 9 Comparison of water elevation along the cut at y=-0.3 *m* for different grids for $\beta = 6°$ at $F_n = 0.28$.

For pure sway and pure yaw the time history of non-dimensional transverse force and yaw moment are shown in Figs. 10 and 11 for different mesh condition, respectively. As can be seen, the results of fine and medium grid are close and therefore to decrease the computational time, medium grid are applied to simulate maneuvering tests. It should be noted that in Fig. 11 the difference between fine and medium grids results is due to transient characteristics of the solution and disappeared when the wave pattern are created around the hull.

Difference between the simulation results of fine grids and medium grids are shown in Table 5. It is seen that the change is approximately 1.6-6%, 1.3-7.7% and 2.3-7.5% for OTT, pure sway and pure yaw, respectively, but the computational time is significantly increased from medium to fine grids. Therefore, the medium grid is applied throughout this study to obtain solutions with minimum computational effort.
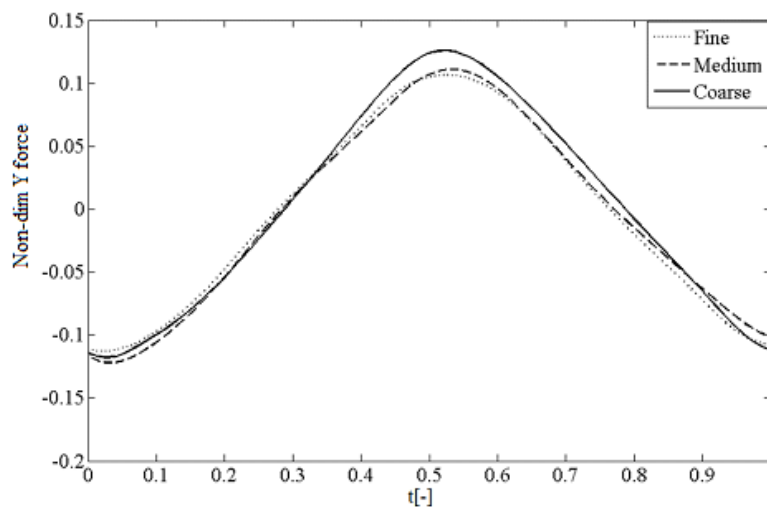

Fig. 10 Time-history of non-dimensional transverse force for pure sway with $v_{max} = 0.266$ *m/s* for different mesh conditions.
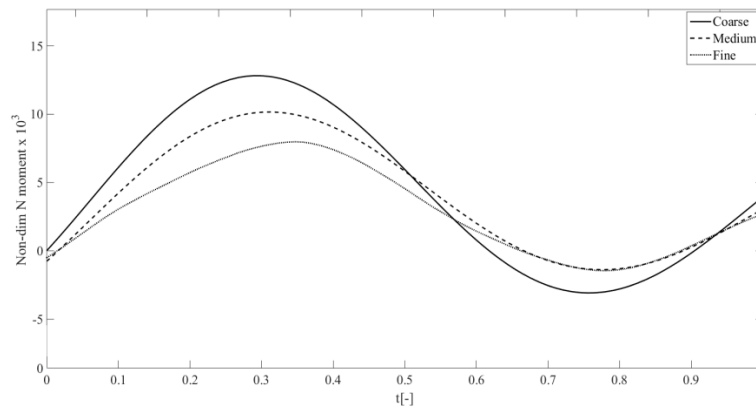
Fig. 11 Time-history of non-dimensional yaw moment for pure yaw with
$r_{max} = 0.450$ *rad/s* for different mesh conditions.

Table 5 difference between fine and medium results.

Condition	E % X'	E % Y'	E % N'
OTT	2.3	1.6	6.0
Pure sway	7.7	1.3	2.7
Pure yaw	7.5	2.9	2.3

The time step convergence is studied for medium mesh for OTT simulation as a stationary case. The simulation is performed using a sequence of monotonically decreasing time-steps from 0.08-0.005 seconds. The calculated non-dimensional forces and moment coefficients for different time step are shown in Table 6. Moreover, the predicted water elevation along the plane at y=-0.3 *m* for different time-steps is compared in Fig. 12. It is seen that difference between the water elevations of different time step is not significantly. For final OTT simulations the time step dt = 0.030 second is applied.
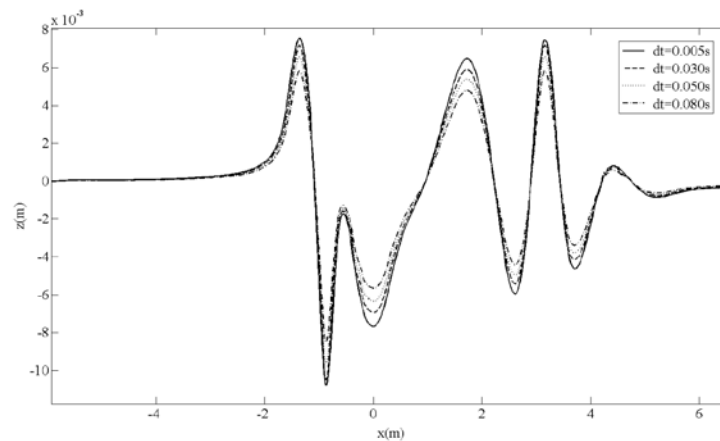

Fig. 12 Comparison of water elevation along the cut at y = -0.3 *m* for different grids for $\beta = 6°$ at $F_n = 0.28$.

Table 6 Dimensionless forces and moment for different time step (OTT).

Time step	X'	Y'	N'
0.080	-0.01831	0.02874	0.01274
0.055	-0.01794	0.02928	0.01357
0.030	-0.01765	0.02977	0.01325
0.005	-0.01740	0.03160	0.01333

Temporal sensitivity analysis for pure yaw and pure sway as harmonic tests are also performed using a sequence of mono-tonically decreasing time-steps from 0.025-0.001 seconds. The calculated non-dimensional forces and moment coefficients for different time step are shown in Table 7.

Table 7 Dimensionless forces and moment for different grid (PMM).

Time step	Pure sway			Pure yaw		
	X'_{max}	Y'_{max}	N'_{max}	X'_{max}	Y'_{max}	N'_{max}
0.0250	0.01977	0.11163	0.02732	0.00946	0.00737	0.00464
0.0175	0.01973	0.11093	0.02682	0.00900	0.00705	0.00461
0.0100	0.01908	0.11123	0.02669	0.00877	0.00764	0.00434
0.0025	0.01871	0.11027	0.02615	0.00820	0.00817	0.00409

It should be noted that the suitable time step for a PMM test is dependent to the motion frequency for final dynamic PMM simulations the time step dt = 0.010 second is applied.

COMPUTATIONAL FLUID DYNAMIC SIMULATIONS

PMM tests are simulated in a CFD environment to predict the hydrodynamic coefficients. All simulations are done in Star-CCM+ software. OTT, pure sway test and pure yaw test are simulated to obtain various hydrodynamic derivatives in (4), (5) and (6). Transverse velocity dependent derivatives X_{vv}, Y_v, Y_{vvv}, N_v, and N_{vvv} are obtained by simulating OTT at various drift angles. All derivatives with respect to the transverse velocity and acceleration are calculated by simulating the pure sway test. However, the sway velocity dependent coefficients obtained by pure sway test are frequency dependent and sway velocity dependent coefficients obtained by OTT are more accurate.

The derivatives with respect to the yaw velocity and acceleration such as Y_r, N_r, $Y_{\dot{r}}$ and $N_{\dot{r}}$, are determined from the pure yaw test.

The coordinates of the body motion are for all tests as follows in earth-fixed coordinate system that are shown in Fig. 2.

$$
\begin{aligned}
x_E &= Ut \\
y_E &= -y_{max} \sin \omega t \\
\psi &= -\arctan(\varepsilon \cos \omega t) + \beta
\end{aligned}
\tag{18}
$$

where ε is the maximum tangent of the trajectory defined as

$$
\varepsilon = \left(\frac{dy}{dx} \right)_{max} = \left(\frac{dy/dt}{dx/dt} \right)_{max} = \frac{y_{max}\omega}{U}
\tag{19}
$$

The components of velocity vector in earth-fixed and body-fixed is given in Table 8 and 9, respectively, for various PMM test.

Table 8 PMM Motions in the Inertia coordinate.

Motion	OTT	Pure Sway	Pure yaw
u_E	U	U	U
v_E	0	$-y_{max} = \omega \cos \omega t$	$-y_{max} \omega \cos \omega t$
r_E	0	0	$\varepsilon \omega \sin \omega t \cdot \dfrac{1}{1+\varepsilon^2 \cos^2 \omega t}$
$\dot{v}_E$	0	$y_{max} \omega^2 \sin \omega t$	$y_{max} \omega^2 \sin \omega t$
$\dot{r}_E$	0	0	$\varepsilon \omega^2 \cos \omega t \cdot \dfrac{1+\varepsilon^2(1+\sin^2 \omega t)}{\left(1+\varepsilon^2 \cos^2 \omega t\right)^2}$

Table 9 PMM Motions in the body-fixed coordinate.

Motion	OTT	Pure Sway	Pure yaw
u	$U\cos \beta$	U	$U\sqrt{1+\varepsilon^2 \cos^2 \omega t}$
v	$-U\cos \beta$	$-y_{max} \omega \cos \omega t$	0
r	0	0	$\varepsilon \omega \sin \omega t \cdot \dfrac{1}{1+\varepsilon^2 \cos^2 \omega t}$
$\dot{v}$	0	$y_{max} \omega^2 \sin \omega t$	0
$\dot{r}$	0	0	$\varepsilon \omega^2 \cos \omega t \cdot \dfrac{1+\varepsilon^2(1+\sin^2 \omega t)}{\left(1+\varepsilon^2 \cos^2 \omega t\right)^2}$

PMM simulations are performed for three different speeds corresponding to F_n = 0.138, 0.280, and 0.410, which are the low, medium, and high speed condition, respectively. The simulations for the OTT and PMM are done based on the model test program that has been proposed by Iowa Institute of Hydraulic Research (IIHR) as shown in Tables 10, 11, respectively (Yoon, 2009).

Table10 Test program for OTT simulations.

F_n	Drift Angle β (deg)
0.138	±0, 2, 6, 9, 10, 11, 12, 16, 20
0.280	±0, 2, 6, 9, 10, 11, 12, 16, 20
0.41	±0, 2, 6, 9, 10, 11, 12

Table 11 Test program for PMM simulations.

Test	Froude number F_n	Maximum sway vel v_{max}	Maximum yaw rate r_{max}	motion frequency ω
Pure sway	0.28	0.053		0.841
		0.107		0.841
		0.266		0.841
Pure yaw	0.28		0.025	0.841
			0.075	0.841
			0.150	0.841
			0.225	1.08
			0.300	1.08
			0.375	1.08

Simulation of OTT

OTT or Pure drift test is done with a constant inflow speed of U at various drift angles β. The components of the flow velocity along the $x-$ and $y-$ axis are $u = U\cos\beta$ and $v = -U\sin\beta$. The body is acted by a hydrodynamic force with components X and Y along the longitudinal and transverse axes respectively. The body is also acted by a moment N about the vertical axis z. If the initial condition is defined when the drift angle β is zero and considering the port and starboard symmetry, Eqs. (4), (5) and (6) is simplified as follows.

$$X = X_{vv}v^2$$

$$Y = Y_v v + Y_{vvv}v^3 \qquad\qquad (20)$$

$$N = N_v v + N_{vvv}v^3$$

By using a curve fitting to the forces and moment data as a function of β, the hydrodynamic derivatives $X_{vv}, Y_v, Y_{vvv}, N_v$ and N_{vvv} are obtained. Predicted wave patterns for OTT are shown in Figs. 13 to 15 for $\beta = 9$ degree at $F_n = 0.138$, 0.28 and 0.41, respectively. The contours in these figures are the isoelevation lines. The water elevation around the body changes in a linear pattern and by increasing the inflow velocity the water elevation increased. Predicted wave patterns are shown in Figs. 16 to18 for $\beta = 6, 11$ and 16 degree at $F_n = 0.28$, respectively. The contours in these figures are the isoelevation lines. The water elevation around the body is increased by increasing the drift angle.
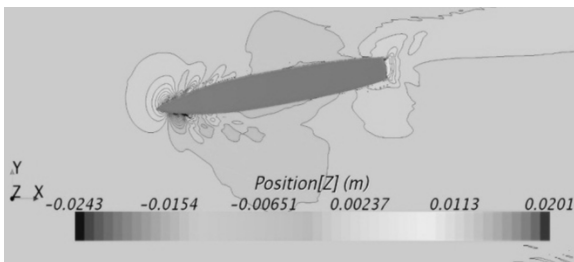
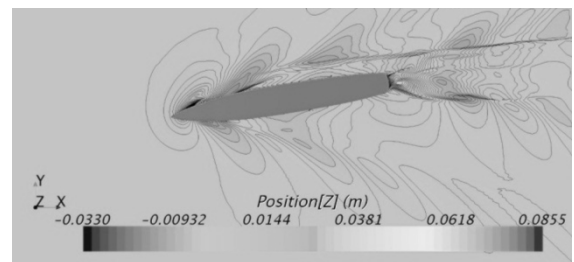Fig. 13 Predicted wave pattern for $\beta = 9°$ at $F_n = 0.138$.

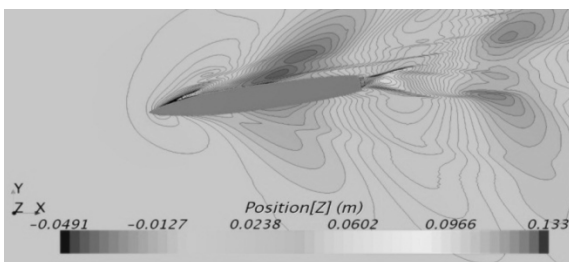Fig. 14 Predicted wave pattern for $\beta = 9°$ at $F_n = 0.28$.

Fig. 15 Predicted wave pattern for $\beta = 9°$ at $F_n = 0.41$.
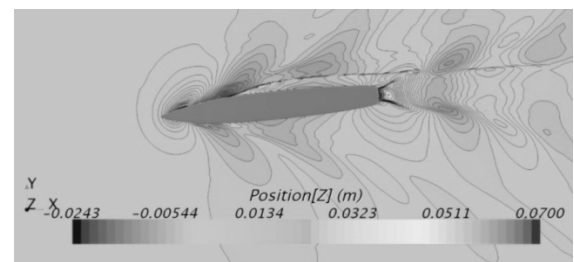

Fig. 16 Predicted wave pattern for $\beta = 9°$ at $F_n = 0.28$.

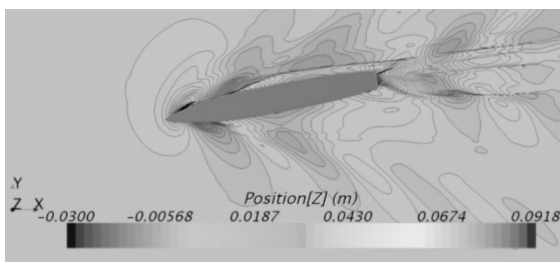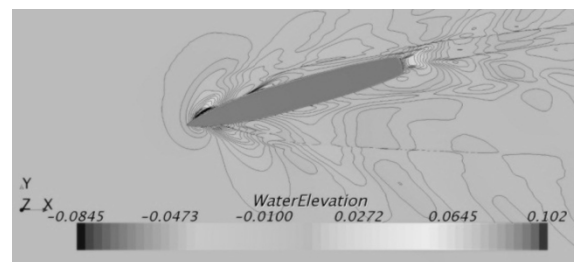Fig. 17 Predicted wave pattern for $\beta = 11°$ at $F_n = 0.28$.

Fig. 18 Predicted wave pattern for $\beta = 16°$ at $F_n = 0.28$.

Time mean values for non-dimensional longitudinal and transverse forces are shown in Figs. 19 and 20 as a function of drift angle β for $F_n = 0.138$, 0.28 and 0.41. Data are fitted to a quadratic and cubic polynomial, respectively. The experimental results (Yoon, 2009) are also depicted in these figures for comparison.
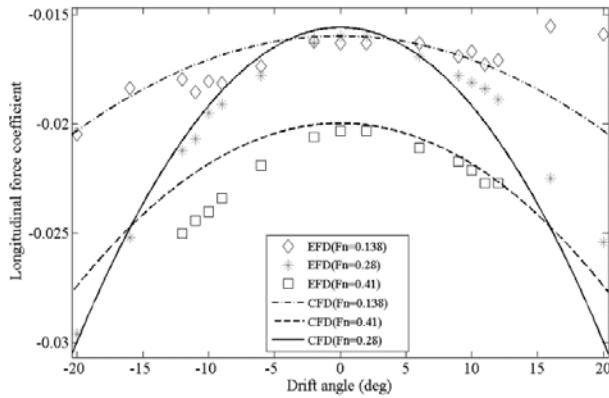

Fig. 19 Computed and experimental time-mean of non-dimensional longitudinal forces, for pure drift for $F_n = 0.138$, 0.280, and 0.410.
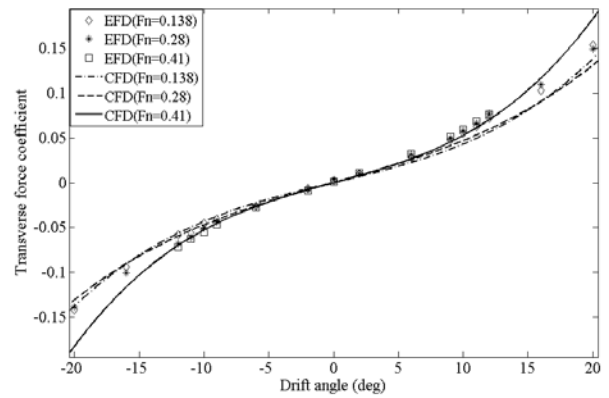
Fig. 20 Computed and experimental time-mean of non-dimensional transverse forces, for pure drift for $F_n = 0.138$, 0.280, and 0.410.

The solutions for non-dimensional longitudinal force should be symmetrically about $\beta = 0$ for identical drift angle to port or to starboard due to the symmetrical shape of the body. The experimental solutions do not show such a trend at $F_n = 0.138$. The non-dimensional transverse force should have identical value with different sign for identical drift angle to port and starboard due to the symmetrical shape of the body. The experimental data show also such a trend approximately. The solver gives accurate results for non-dimensional transverse force in compare with Experimental Fluid Dynamic (EFD) results.

The non-dimensional yaw moment is also depicted in Fig. 21 as a function of β for $F_n = 0.138$, 0.28 and 0.41. Data are fitted to a cubic polynomial. The $N - \beta$ graph should demonstrate a symmetrical shape with respect about $\beta = 0$. The experimental results show approximately such a trend as depicted in Fig. 21. The solver gives accurate results in compare with EFD.
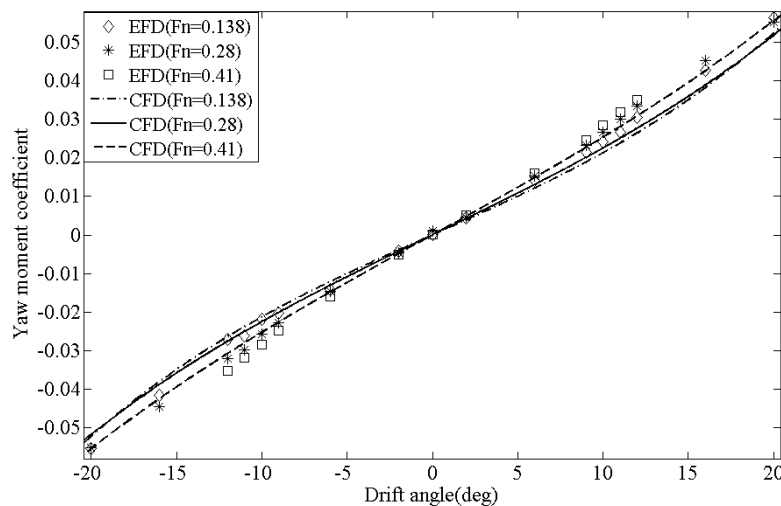

Fig. 21 Computed and experimental time-mean of non-dimensional yaw moments for pure drift for $F_n = 0.138$, 0.280, and 0.410.

The derivatives Y_v and N_v can be obtained from the transverse force and yaw moment curves against β from chain rule as follows.

$$Y_v = \frac{\partial Y}{\partial \beta}\Bigg|_{\beta=0} \frac{\partial \beta}{\partial v}\Bigg|_{v=0} = \frac{1}{U} \frac{1}{\sqrt{1-\left(\dfrac{v}{U}\right)^2}}\Bigg|_{v=0} \quad Y_\beta\Big|_{\beta=0} = \frac{1}{U}Y_\beta \tag{21}$$

$$N_v = \frac{\partial N}{\partial \beta}\Bigg|_{\beta=0} \frac{\partial \beta}{\partial v}\Bigg|_{v=0} = \frac{1}{U}N_\beta\Big|_{\beta=0} \tag{22}$$

The derivatives Y_β and N_β are the slope of the transverse force and yaw moment curves against drift angle at $\beta = 0$. The values of Y_v and N_v are obtained using (21, 22) and are given in Table 12 for $F_n = 0.138$, 0.28 and 0.41 The experimental values of these derivatives are also tabulated for comparison. Difference between the solver results and EFD are shown in Table 13.

Table 12 Linear hydrodynamic coefficients (Pure drift simulation).

Coefficients	$F_n = 0.138$		$F_n = 0.28$		$F_n = 0.41$	
	CFD	EFD	CFD	EFD	CFD	EFD
Y_v	-0.2385	-0.2637	-0.2672	-0.2961	-0.3215	-0.2963
N_v	-0.1458	-0.1396	-0.1589	-0.1667	-0.1654	-0.1717

Table 13 difference between EFD and CFD for linear HDC.

	$F_n = 0.138$	$F_n = 0.28$	$F_n = 0.41$
Coefficients error			
E % Y_v	9.56	9.76	8.50
E % N_v	4.44	4.68	3.67

The nonlinear derivatives X_{vv}, Y_{vv} and N_{vvv} are obtained from the longitudinal and transverse forces and yaw moment curves against β by using chain rule of differentiation.

$$X_{vv} = \frac{\partial^2 X}{\partial \beta^2}\Bigg|_{\beta=0} \left(\frac{\partial \beta}{\partial v}\right)^2 = \left(\frac{1}{U}\right)^2 X_{\beta\beta}\Big|_{\beta=0} \tag{23}$$

$$Y_{vv} = \frac{\partial^3 Y}{\partial \beta^3}\Bigg|_{\beta=0} \left(\frac{\partial \beta}{\partial v}\right)^3 = \left(\frac{1}{U}\right)^3 Y_{\beta\beta\beta}\Big|_{\beta=0} \tag{24}$$

$$N_{vv} = \frac{\partial^3 N}{\partial \beta^3}\Bigg|_{\beta=0} \left(\frac{\partial \beta}{\partial v}\right)^3 = \left(\frac{1}{U}\right)^3 N_{\beta\beta\beta}\Big|_{\beta=0} \tag{25}$$

The nonlinear derivative $X_{\beta\beta}$ is obtained by finding the second derivative of the longitudinal force curve against drift angle at $\beta = 0$. This can be obtained by using a curve fitting and finding the second derivatives of the fitted curve. The derivatives $Y_{\beta\beta\beta}$ and $N_{\beta\beta\beta}$ are also obtained by calculating the third-order derivative of the transverse force and yaw moment curves against drift angle at $\beta = 0$. These are obtained by using curve fittings to the related data. The solutions for these deri-

vatives are given in Table 14 for $F_n = 0.138$, 0.28 and 0.41. The experimental results are also given in Table 14 for comparison. Difference between the numerical results and EFD for nonlinear hydrodynamic coefficients is shown in Table 15.

Table 14 Nonlnear hydrodynamic coefficients (OTT simulation).

Coefficients	$F_n = 0.138$		$F_n = 0.28$		$F_n = 0.41$	
	CFD	EFD	CFD	EFD	CFD	EFD
X_{vv}	-0.0339	-0.0301	-0.1694	-0.1528	-0.1751	-0.1544
Y_{vvv}	-1.5234	-1.6256	-1.7584	-1.9456	-3.582	-3.7963
N_{vvv}	-0.3251	-0.3426	-0.4047	-0.4355	-1.1941	-1.2591

Table 15 difference between EFD and CFD for Nonlinear HDC.

	$F_n = 0.138$	$F_n = 0.28$	$F_n = 0.41$
Coefficients error			
E % X_{vv}	12.62	10.86	13.41
E % Y_{vvv}	6.29	9.62	5.64
E % N_{vvv}	5.11	7.07	5.16

Simulation of dynamic PMM tests

Pure sway and pure yaw tests are also simulated in CFD environment. The yaw angular velocity in pure sway test is zero and Eqs. (4), (5) and (6) are simplified as follows.

$$X = X_{vv} v^2$$
$$Y = Y_{\dot{v}} \dot{v} + Y_v v + Y_{vvv} v^3 \tag{26}$$
$$N = N_{\dot{v}} \dot{v} + N_v v + N_{vvv} v^3$$

The transverse velocity is zero in pure yaw motion and the hydrodynamic forces and moments are as follows according to Eqs. (4) to (6).

$$X = X_{rr} r^2$$
$$Y = Y_{\dot{r}} \dot{r} + Y_r r + Y_{rrr} r^3 \tag{27}$$
$$N = N_{\dot{r}} \dot{r} + N_r r + N_{rrr} r^3$$

If the time-histories of hydrodynamic forces and moment are obtained during the simulations then the hydrodynamic derivatives in (26) and (27) can be computed. By replacing corresponding surge, sway and yaw velocities and accelerations given in Table 9 in body-fixed reference frame into Eqs. (26) and (27), the following general sinusoidal functions are obtained for hydrodynamic forces and moment for both pure sway and yaw motions.

Pure sway:

$$X = A_1 + A_2 \cos 2\omega t$$
$$Y = B_1 \cos \omega t + B_2 \sin \omega t + B_3 \cos 3\omega t \tag{28}$$
$$N = C_1 \cos \omega t + C_2 \sin \omega t + C_3 \cos 3\omega t$$

where

$$A_1 = \frac{1}{2} X_{vv} v_{max}^2$$

$$A_2 = \frac{1}{2} X_{vv} v_{max}^2$$

$$B_1 = -\left(Y_v v_{max} + \frac{3}{4} Y_{vvv} v_{max}^3 \right)$$

$$B_2 = Y_{\dot{v}} \dot{v}_{max}$$

$$B_3 = -\frac{1}{4} Y_{vvv} v_{max}^3$$

$$C_1 = -\left(N_v v_{max} + \frac{3}{4} N_{vvv} v_{max}^3 \right)$$

$$C_2 = N_{\dot{v}} \dot{v}_{max}$$

$$C_3 = -\frac{1}{4} N_{vvv} v_{max}^3$$

(29)

Pure yaw:

$$X = A_1 + A_2 \cos 2\omega t$$

$$Y = B_1 \sin \omega t + B_2 \cos \omega t + B_3 \sin 3\omega t$$

$$N = C_1 \sin \omega t + C_2 \cos \omega t + C_3 \sin 3\omega t$$

(30)

where

$$A_1 = \frac{1}{2} X_{rr} r_{max}^2$$

$$A_2 = -\frac{1}{2} X_{rr} r_{max}^2$$

$$B_1 = Y_r r_{max} + \frac{3}{4} Y_{rrr} r_{max}^3$$

$$B_2 = Y_r \dot{r}_{max}$$

$$B_3 = -\frac{1}{4} Y_{rrr} r_{max}^3$$

$$C_1 = N_r r_{max} + \frac{3}{4} N_{rrr} r_{max}^3$$

$$C_2 = N_r \dot{r}_{max}$$

$$C_3 = -\frac{1}{4} N_{rrr} r_{max}^3$$

(31)

By fitting (28) and (30) to the time-histories of forces and moment computed from pure sway and pure yaw, respectively, the hydrodynamic derivatives or coefficients are obtained.

The volume fraction distributions are shown in Fig. 22 at bow at various times during the pure sway test simulation. The volume fraction distribution simulates the elevation of free surface of the water. In other word, the figure shows the wave formation on the bow of the model ship. There is no wave formation and the free surface is flat at $\omega t = 0$. The wave has a symmetrical form on both sides of the model at $\omega t = \pi/2$. The water elevation has a symmetrical form at $\omega t = \pi/4$ and $3\pi/4$. The wave pattern is also depicted in Fig. 23 around the body at various times during the pure sway test simulation. The trend of wave pattern is the same as volume fraction distiribution shown in Fig. 22.
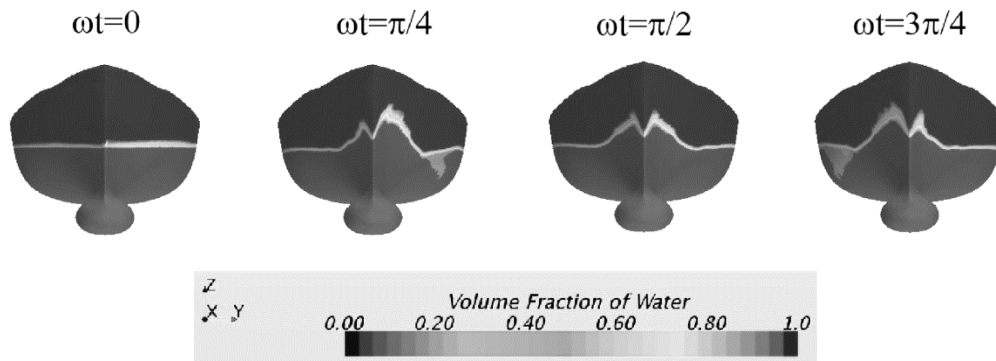
Fig. 22 Predicted water volume fraction for pure sway ($F_n = 0.28$, $V_{max} = 0.107$ *m/s*, $\omega = 0.841$ *rad/s*) at $\omega t = 0, \pi/4, \pi/2, 3\pi/4$.

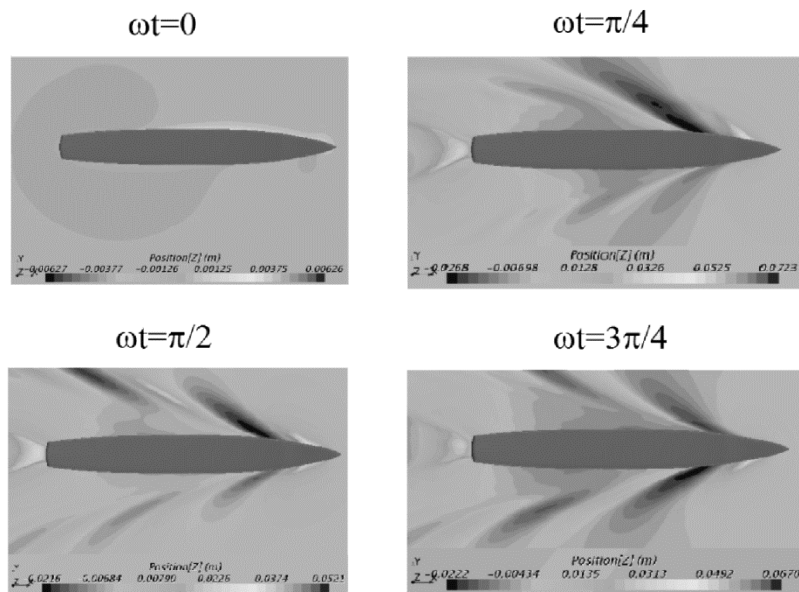

Fig. 23 Predicted wave pattern for pure sway ($F_n = 0.28$, $V_{max} = 0.107$ *m/s*, $\omega = 0.841$ *rad/s*) at $\omega t = 0, \pi/4, \pi/2, 3\pi/4$.

Time-histories of the longitudinal and transverse hydrodynamic forces of the pure sway PMM motion for three different maximum sway velocities, v_{max} =0.053 *m/s*, 0.107 *m/s* and 0.266 *m/s*, at $F_n = 0.28$ are shown in Figs. 24 and 25, respectively. Data are fitted to a general sinusoidal function of X and Y as given in (28). As can be seen although the pattern change of the forces is same for different transverse velocities but by increasing the sway velocity the amplitude of hydrodynamic forces are increased. Time histories of the yaw moment of the pure sway for three different maximum velocities, $v_{max} = 0.053$ *m/s*, 0.107 *m/s* and 0.266 *m/s*, at $F_n = 0.28$ are shown in Fig. 26. Data are fitted to a general sinusoidal function of N as (28). The yaw moment also demonstrates a general sinusoidal pattern. The amplitude of the yaw moment increases as the sway velocity amplitude is increased. The frequency of the motion is kept constant during all simulations and is equal to 0.841 *rad/s*.
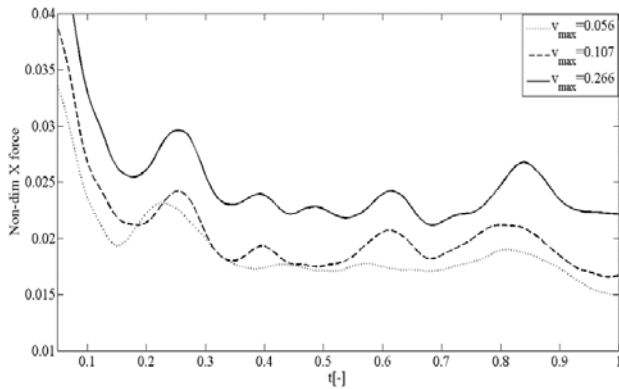
Fig. 24 Computed time-histories of non-dimensional longitu-
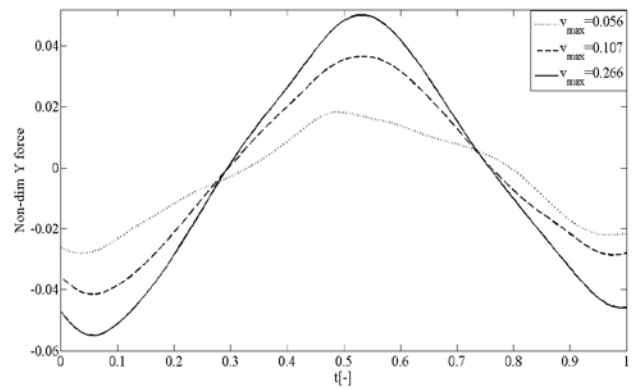dinal force for pure sway for different sway velocities.

Fig. 25 Computed time-histories of non-dimensional trans-
verse force for pure sway for different sway velocities.
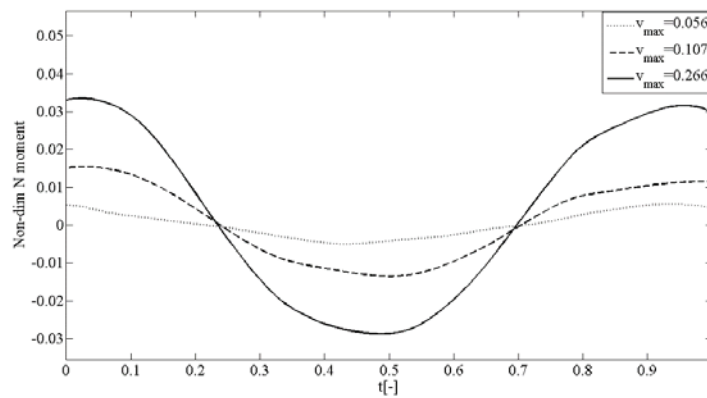

Fig. 26 Computed time-histories of non-dimensional yaw moment for pure sway for different sway velocities.

Hydrodynamic coefficients are calculated for three pure sway simulations. The Root Mean Squre (RMS) value of theses coefficients are considered as pure sway hydrodynamic coefficients. They are presented in Table 16 where the experimental data are also given. The error between the CFD solutions and EFD are different for various coefficent and it changes from 5 to 21 percent.

Table 16 Hydrodynamic coefficients (pure sway simulation).

Coefficients	$F_n = 0.28$	
	CFD	EFD
X_{vv}	-0.1177	-0.1421
Y_v	-0.2531	-0.3000
Y_{vvv}	-1.6411	-1.7875
N_v	-0.1731	-0.1628
N_{vvv}	-0.2837	-0.3284
$Y_{\dot{v}}$	-0.1361	-0.1111
$N_{\dot{v}}$	-0.0153	-0.0131

The volume fraction distributions are shown in Fig. 27 at bow at various times during the yaw test simulation. The trend of the volume fraction distribution is different than the sway test simulations, depicted in Fig. 22. It can be seen also in Fig. 28 where the wave patterns around the body are depicted for yaw test simulations. The water elevation is higher on the starboard side where is the inner side, during the test.
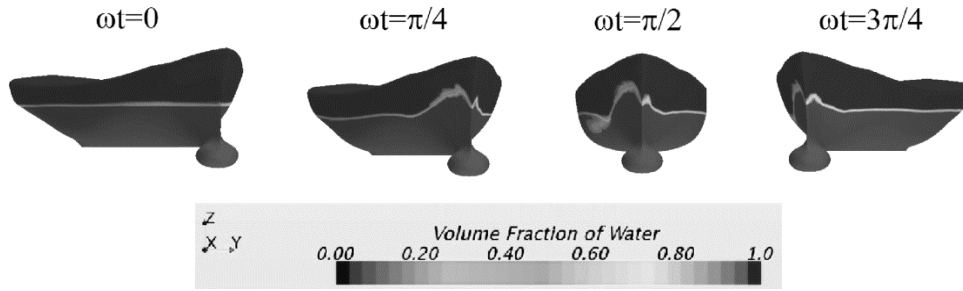
Fig. 27 Predicted water volume fraction for pure yaw ($F_n = 0.28$, $v_{max} = 0.107$ *m/s*, $\varpi = 0.841$ *rad/s*) at $\omega t = 0, \pi/4, \pi/2, 3\pi/4$.
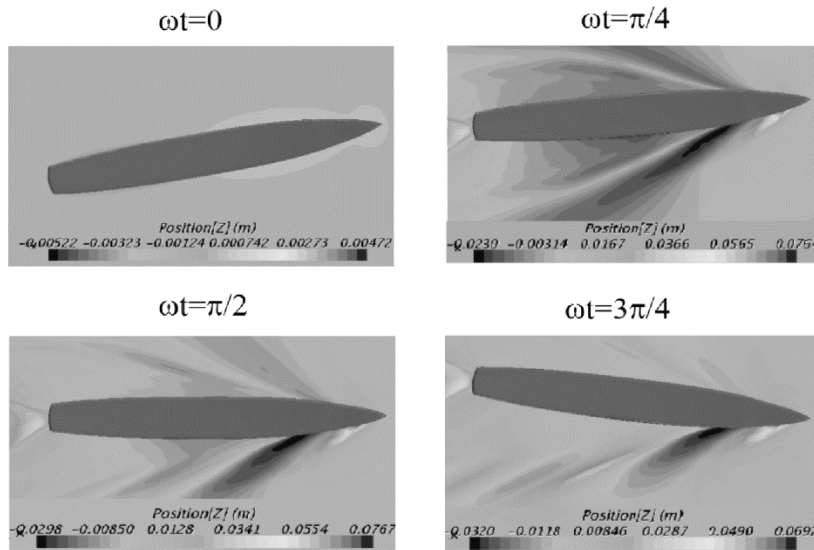

Fig. 28 Predicted wave pattern for pure yaw ($F_n = 0.28$, $v_{max} = 0.107$ *m/s*, $\varpi = 0.841$ *rad/s*) at $\omega t = 0, \pi/4, \pi/2, 3\pi/4$.

Time-histories of the hydrodynamic forces and moment are computed by simulation of pure yaw tests on DTMB model ship for six different yaw rate amplitude, $r_{max} = 0.025, 0.075, 0.150, 0.225, 0.300, 0.375$ *rad/s*, and two frequencies, 0.841 *rad/s* and 1.08 *rad/s*, at $F_n = 0.28$. The results of computations are shown in Figs. 29 and 30 for longitudinal and transverse forces, respectively. The solutions for yaw moment are given in Fig. 31. The hydrodynamic derivatives are obtained by fitting general sinusoidal functions to data obtained for hydrodynamic forces and moments according to (30).
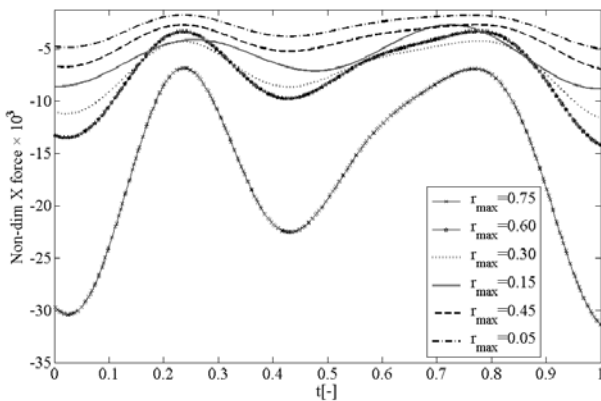

Fig. 29 Computed time-histories of non-dimensional longitudinal force for pure yaw for different yaw rate.
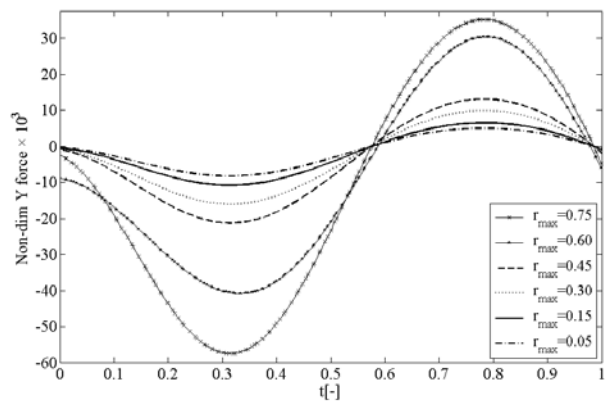
Fig. 30 Computed time-histories of non-dimensional transverse force for pure yaw for different yaw rate.
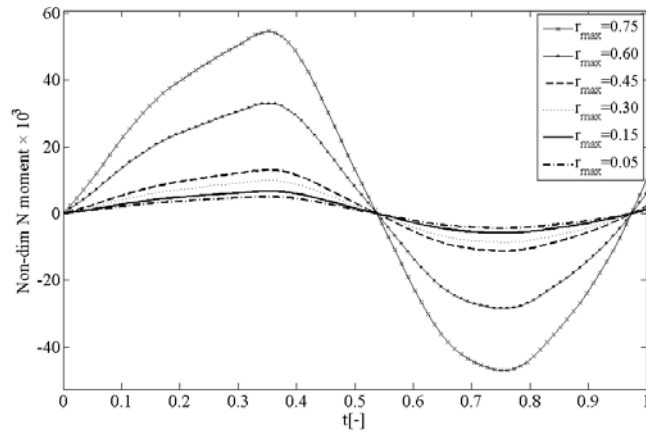
Fig. 31 Computed time-histories of non-dimensional yaw moment for pure yaw for different yaw rate.

The RMS values of the pure yaw coefficients are presented in Table 17. The CFD solutions for pure yaw motion are comply more with EFD than pure sway motion. The relative errors between various coefficients are changes from 2 to 13 percent.

Table 17 Hydrodynamic coefficients (pure yaw simulation).

Coefficients	$F_n = 0.28$	
	CFD	EFD
X_{rr}	-0.0264	-0.0282
Y_r	-0.0482	-0.0485
Y_{rrr}	-0.4169	-0.4520
N_r	-0.0504	-0.0485
N_{rrr}	-0.0473	-0.0505
$Y_{\dot{r}}$	-0.0102	-0.0090
$N_{\dot{r}}$	-0.0068	-0.0070

Maneuvering Simulation based on CFD data

The classification societies assign some standard maneuvers to evaluate the maneuvering qualities of a marine vehicle. The steady turning and zig-zag maneuvers are the maneuvers that are designed to provide the turning, yaw checking and course-keeping abilities of a marine vehicle. Steady turning maneuver is done at a desired speed by deflecting the rudder to a maximum angle (35 *deg*) to port or starboard from a zero yaw angle until a steady turning circle is obtained. Tactical diameter, advance, transfer and steady turning radius are the essential parameters that are obtained from this maneuver. Zig-zag maneuver is done by deflecting the rudder angle to a desired angle such as 20° to port or starboard and keep it until heading angle approach to 20° then the rudder angle is shifted to other side. Overshoot angles and initial turning time to second execute are essential parameters that are obtained from the zig-zag maneuver.

The simulations of these two maneuvers are obtained through the solution of the system of differential Eqs. (1) to (3). These equations may be given using the Taylor series expansion as follows.

$$m(\dot{u} - rv) = X_u(u - U) + X_{uu}(u - U)^2 + X_{rr}r^2$$
$$+ X_{vv}v^2 + X_{vr}vr + X_{vvu}v^2u + X_{rru}r^2u$$

(32)

$$(m - Y_{\dot{v}})\dot{v} + (mx_G - Y_{\dot{r}})\dot{r} = Y_v v + \frac{1}{6}Y_{vvv}v^3 + \frac{1}{2}Y_{vrr}vr^2$$
$$+ Y_{vu}v(u - U) + (Y_r - mU)r \tag{33}$$
$$+ \frac{1}{6}Y_{rrr}r^3 + \frac{1}{2}Y_{rvv}rv^2 + Y_\delta\delta + \frac{1}{6}Y_{\delta\delta\delta}\delta^3$$

$$(mx_G - N_{\dot{v}})\dot{v} + (I_Z - N_{\dot{r}})\dot{r} = N_v v + \frac{1}{6}N_{vvv}v^3 + \frac{1}{2}N_{vrr}vr^2$$
$$+ N_{vu}v(u - U) + (N_r - mU)r \tag{34}$$
$$+ \frac{1}{6}N_{rrr}r^3 + \frac{1}{2}N_{rvv}rv^2 + N_\delta\delta + \frac{1}{6}N_{\delta\delta\delta}\delta^3$$

The parameter δ is rudder angle and Y_δ, $Y_{\delta\delta\delta}$, N_δ and $N_{\delta\delta\delta}$ are the various order derivatives of transverse force and yaw moment with respect to the rudder angle. All derivatives are obtained for the CFD simulation of OTT, pure yaw and pure sway tests except the cross coupling coefficients such as Y_{vrr}, Y_{vu} and N_{vu}. The cross coupling derivatives are taken from available model test data given in (Yoon, 2009) as shown in Table 18. The mass of the model ship is 86 *kg* and the mass moment of inertia is 49.99 *kgm²* (Yoon, 2009).

Table 18. Hydrodynamic derivatives of Steering equation (Yoon, 2009).

X_u	-0.0087
X_{uu}	-0.0205
X_{rr}	-0.0190
X_{vv}	-0.1421
X_{vr}	0.0300
X_{vvu}	-0.0903
X_{rru}	-0.0094
Y_{vrr}	-1.3683
Y_{vu}	-0.0242
Y_{vvr}	-1.7067
Y_δ	0.0586
$Y_{\delta\delta}$	-0.0097
N_{vrr}	-0.4011
N_{vu}	-0.0397
N_{vvr}	-0.5512
N_δ	-0.0293
$N_{\delta\delta}$	0.0048

To calculate the ship path during each maneuver, initial values for v, r and δ are set to zero. A time step such as *h* is considered and the new values for *v,r* at time $t_1 = t_0 + h$ are found from the solution of (33) and (34). The solution of (32) to (34) can be obtained by various methods such as Euler algorithm, Runge-Kutta (4th order) method, Runge-Kutta method with variable time step (5th order) and predictor-corrector method. The procedure is repeated using the values of *v, r* at time t_n to obtain the new *v, r* for a time $t_{n+1} = t_n + h$ and so on. The difference of turning and zig-zag maneuver is about definition of the rudder deflection as a function of time. To simulate turning maneuver the rudder deflects with constant deflection rate 0.04

rad/s up to maximum rudder angle, 35 *deg*, and then rudder angle set to this angle. But for zig-zag maneuver first rudder deflects with constant rate 0.04 *rad/s* up to 20 *deg* and keep it until the ship heading achieved 20 *deg*. After that the rudder is deflected to other side.

The Fourth-order Runge-Kutta method and Euler algorithm are applied to simulate the turning and zig-zag maneuvers, respectively. The time step is set to be equal to h=0.1 *sec.* in simulation of the maneuvers. After finding the values of *v, r* for each maneuver at various times *t*, the yaw angle and the position of the ship relative to a fixed coordinate system are calculated by numerical integration of the following equations during each maneuver.

$$\psi(t) = \int_0^t r(t)dt$$
$$x(t) = \int_0^t \big(u(t)\cos\psi(t) - v(t)\sin\psi(t)\big)dt \tag{35}$$
$$y(t) = \int_0^t \big(u(t)\sin\psi(t) + v(t)\cos\psi(t)\big)dt$$

The resultant trajectory is shown for turning path in Fig 32. The yaw rate and speed changing in turning circle simulation are shown in Fig. 33. The numerical simulations have a good accuracy and are close to the experimental results that are given in Figs. 32 and 33. The resultant trajectory of zig-zag maneuver is shown in Fig. 34. The numerical simulation of zig-zag maneuver is complying with EFD.
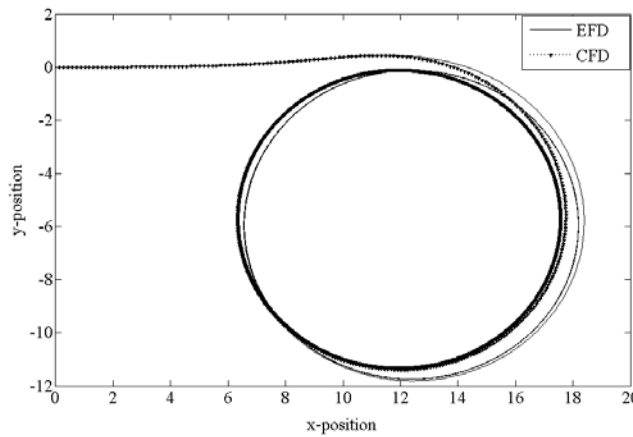

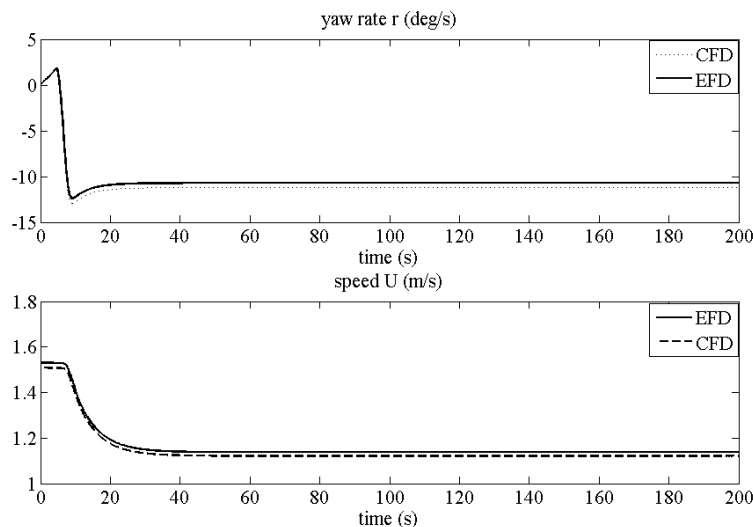Fig. 32 Simulation of turning circle of ship with δ = 35 *deg*.

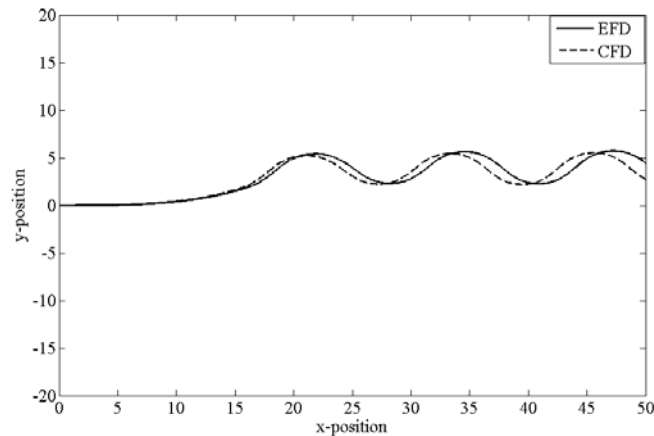Fig. 33 Yaw rate and speed in a turning circle simulation.

Fig. 34 Simulation of 20/20 *deg* zig-zag of ship.

CONCLUSION

Maneuverability is an important hydrodynamic quality of a marine vehicle. The maneuvering characteristics of a marine vehicle should be predicted during the various design stages and validated after construction of the vessel during the trial tests. There are various mathematical models to predict the maneuvering properties of a marine vehicle and the Abkowitz model is one of them. In Abkowitz model, the external forces and moments are defined using hydrodynamic derivatives or coefficients based on Taylor series expansion. These hydrodynamic coefficients should be found in advance to predict the maneuvering properties of a marine vehicle. CFD is used to found these hydrodynamic coefficients of a model ship by virtual simulating PMM test. The simulations are done using the RANS code STAR-CCM+.

OTT and dynamic PMM tests are simulated for various conditions similar to experimental PMM tests program that conducted in IIHR towing tank. Hydrodynamic forces and moment are calculated during simulation and damping and added mass coefficients are extracted from these data. The results indicate that the force and moment variations are basically nonlinear and therefore both linear and nonlinear coefficients can be derived by CFD computations because CFD can be performed for a wider range of motion variables. The simulations show that the CFD is precise and affordable tool at the preliminary design stage to obtain optimal maneuverability performance.

ACKNOWLEDGMENT

REFERENCES

Abkowitz, M.A., 1969. *Stability and motion control of ocean vehicles*. Massachusetts and London: The M.I.T, Cambridge.

Dantas, J.L.D. and de Barros, E.A., 2013. Numerical analysis of control surface effects on AUV manoeuvrability. *Journal of Applied Ocean Research*, 42, pp.168-181.

Ferziger, H. J. and Peric, M., 2002. *Computational methods for fluid dynamics*. 3rd edition. Berlin: Springer.

Hajivand, A. and Mousavizadegan, S.H., 2015. Virtual maneuvering test in CFD media in presence of free surface. *International Journal of Naval Architecture and Ocean Engineering*, 7(3), pp.540-558.

Hirt, C.W. and Nichols, B.D., 1981. Volume of fluid (VOF) method for the dynamics of free boundaries. *Journal of Computational Physics*, 39, pp.201-225.

International Maritime Organization (IMO), 2002a. *Resolution standards for ship maneuverability, MSC.137 (76)*. London: IMO.

International Maritime Organization (IMO), 2002b. *Explanatory notes to the standards for ship maneuverability, MSC/ Circ 1053*. London: IMO.

Nazir, Z., Su, Y. and Wang, Z., 2010. A CFD based investigation of the unsteady hydrodynamic coefficients of 3-D fins in viscous flow. *Journal of Marine Science and Application*, 9(3), pp.250-255.

Nomoto, K., 1960. Analysis of Kempf's standard maneuver test and proposed steering quality indices. *Proceedings of 1st Symposium on Ship Maneuverability*, Department of the Navy, Maryland, United State of America, 24-25 May 1960, pp.275- 304.

Park, S., Park, S.W., Rhee, S.H., Lee, S.B., Choi, J. and Kang, S.H., 2013. Investigation on the wall function implementation for the prediction of ship resistance. *International Journal of Naval architecture and Ocean Engineering*, 5(1), pp.33-46.

Ray, A., Singh, S.N. and Seshadri, V., 2009. Evaluation of linear and nonlinear hydrodynamic coefficients of underwater vehicles using CFD. *Proceedings of the ASME 28th International Conference on Ocean, Offshore and Arctic Engineering, Honolulu, Hawaii*, 31 May - 5 June 2009, pp.257-265.

Roache, P.J., 1997. Quantification of uncertainty in computational fluid dynamics. *Annual Review of Fluid Mechanics*, 29, pp.123-160.

Sarkar, T., Sayer, P.G. and Fraser, S.M., 1997. A study of autonomous underwater vehicle hull forms using computational fluid dynamics. *International Journal for Numerical Methods in Fluids*, 25(11), pp.1301-1313.

Seo, J.H., Seol, D.M., Lee, J.H. and Rhee, S.H., 2010. Flexible CFD meshing strategy for prediction of ship resistance and propulsion performance. *International Journal of Naval Architecture and Ocean Engineering*, 2(3), pp.139-145.

Simonsen, C.D., Otzen, J.F., Klimt, C., Larsen, N.L. and Stern, F., 2012. Maneuvering predictions in the early design phase using CFD generated PMM data. *29th Symposium on Naval Hydrodynamics*, Gothenburg, Sweden, 26-31 August 2012.

Stern, F., Agdrup, K., Kim, S.Y., Hochbaum, A.C., Rhee, K.P., Quadvlieg, F., Perdon, P., Hino, T., Broglia, R. and Gorski, J., 2011. Experience from SIMMAN 2008—the first workshop on verification and validation of ship maneuvering simulation methods. *Journal of Ship Research*, 55(2), pp.135-147.

Tyagi, A. and Sen, D., 2006. Calculation of transverse hydrodynamic coefficients using computational fluid dynamic approach. *Journal of Ocean Engineering*, 33(5-6), pp.798-809.

Wilson, R., Paterson, E. and Stern, F., 1998. Unsteady RANS CFD method for naval combatants in waves. *Proceedings of 22nd Symposium Naval Hydrodynamic*, Washington, D C., 9-14 August 1998, pp.532-549.

Yoon, H.S., 2009. *Phase-averaged stereo-PIV flow field and Force/moment/motion measurements for surface combatant in PMM maneuvers*. PhD thesis. The University of Iowa.

Yoshimura, Y., 2005. Mathematical model for maneuvering ship motion (MMG Model). *Workshop on Mathematical Models for Operations involving Ship-Ship Interaction*, Tokyo, August 2005, pp.1-6.

Zhang, H., Xu, Y. and Cai, H., 2010. Using CFD software to calculate hydrodynamic coefficients. *Journal of Marine Science and Application*, 9, pp.149-155.